Optical Probe of Magnetic Ordering Structure and Spin-Entangled Excitons in Mn-Substituted NiPS$_3$

Je-Ho Lee, Seungyeol Lee, Youngsu Choi, Lukas Gries, Rüdiger Klingeler,* Kalaivanan Raju, Rajesh Kumar Ulaganathan, Raman Sankar,* Maeng-Je Seong,* and Kwang-Yong Choi*

In van der Waals magnets, the interplay between magneto-excitonic coupling and optical phenomena opens avenues for directly probing magnetic ordering structures, manipulating excitonic properties through magnetic fields, and exploring quantum entanglement between electronic and magnetic states. Notably, NiPS$_3$ stands out for its capacity to host spin-entangled excitons, where the excitonic states are intricately tied with the material's spin configuration. Herein, it is experimentally showcased that the spin-entangled excitons can be utilized for detecting the magnetic easy axis in Ni$_{1-x}$Mn$_x$PS$_3$ (x = 0–0.1). The end members of this series exhibit distinct magnetic ordering patterns and easy axes: zigzag ordering with magnetic moments aligned along the *a*-axis for NiPS$_3$ versus Néel ordering with the out-of-plane easy axis for MnPS$_3$. By combining angle-resolved exciton photoluminescence with magnetic susceptibility measurements, it is observed that the magnetic easy axis rotates away from the local spin chain direction with increasing Mn content. Moreover, through a comprehensive thermal and substitution study, it is demonstrated that the energy and lifetime of spin-entangled excitons are governed by two spin-flip processes and are drastically influenced by disparate electronic states. These findings not only provide optical means to map out magnetic ordering structures but also offer insights into decoherence processes in spin-exciton entangled states.

1. Introduction

Layered van der Waals (2D vdW) antiferromagnets have garnered significant interest due to their relevance to terahertz resonance, ultrafast spin dynamics, and ultrathin spintronic devices.[1–4] In the quest for future opto-spintronic applications, a central theme revolves around the capability to control electronic, lattice, orbital, and magnetic properties through electrical and optical methods. Among the diverse family of vdW antiferromagnets, NiPS$_3$ holds promising potential to implement various functionalities. This is owed to the intimate interplay between its electronic, magnetic, and optical properties, leading to correlated many-body phenomena, hybrid excitations, and composite quasiparticles.[5–11] Furthermore, practical applications such as UV photodetectors, field-effect transistors, and humidity sensors have been actively pursued.[12–15]

The vdW antiferromagnet NiPS$_3$ is a charge-transfer insulator with a band gap of ≈1.8 eV, forming a honeycomb lattice of Ni^{2+} (d^8; S = 1) ions in monoclinic $C2/m$ symmetry. A zig-zag antiferromagnetic order occurs at the Néel temperature $T_N \approx 155$ K,[16–36] where the magnetic moments align ferromagnetically along the crystalline *a*-axis and antiferromagnetically between adjacent zigzag chains in the *ab* layer (see the schematic illustration in **Figure 1a**). On the other hand, NiPS$_3$ exhibits a weak anisotropy along the *b*-axis, while the magnetic moments are slightly tilted toward an out-of-plane direction. Above all, the most striking feature of NiPS$_3$ is the observation of a sharp

J.-H. Lee, S. Lee, M.-J. Seong
Department of Physics and Center for Berry Curvature-based New Phenomena (BeCaP)
Chung-Ang University
Seoul 06974, Republic of Korea
E-mail: mseong@cau.ac.kr

Y. Choi, K.-Y. Choi
Department of Physics
Sungkyunkwan University
Suwon 16419, Republic of Korea
E-mail: choisky99@skku.edu

L. Gries, R. Klingeler
Kirchhoff Institute for Physics
Heidelberg University
69120 Heidelberg, Germany
E-mail: klingeler@kip.uni-heidelberg.de

K. Raju, R. K. Ulaganathan, R. Sankar
Institute of Physics
Academia Sinica
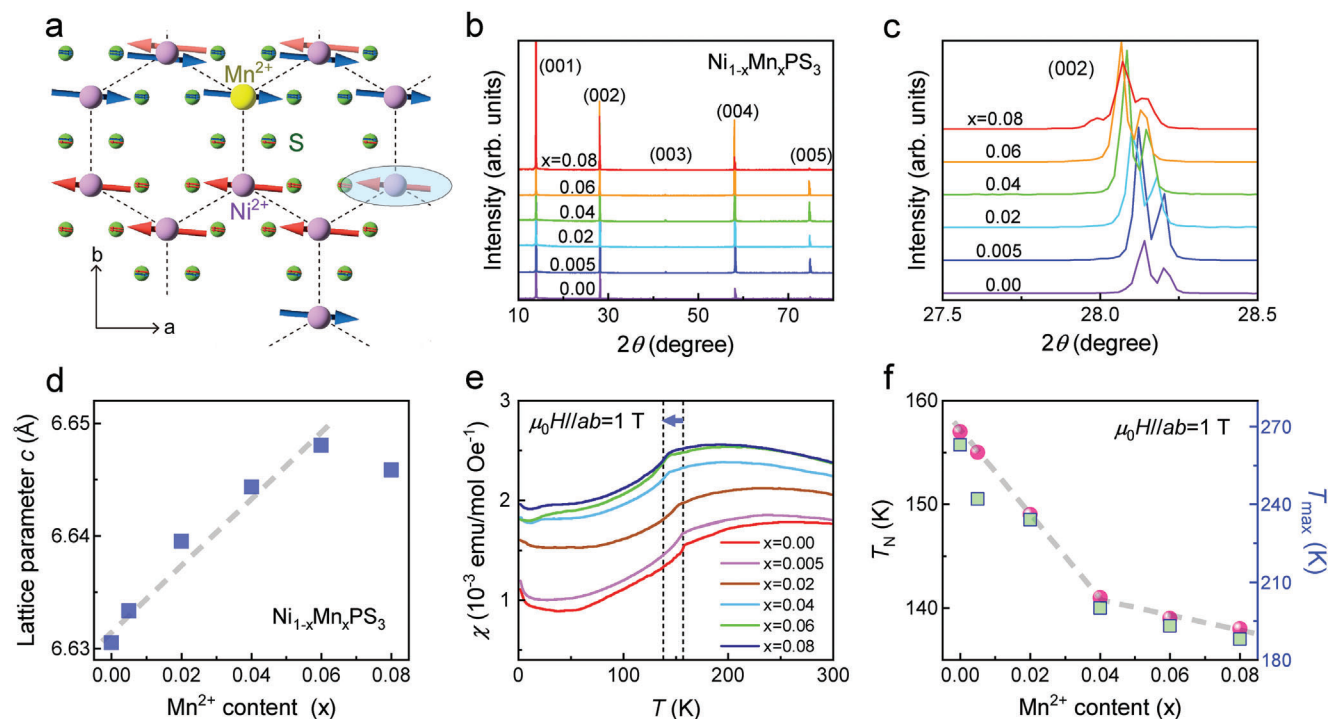Nankang, Taipei 11529, Taiwan ROC
E-mail: sankarraman@gate.sinica.edu.tw

Figure 1. a) Zigzag spin ordering on the honeycomb lattice in $Ni_{1-x}Mn_xPS_3$. The magnetic moments of Ni lie predominantly along the a-axis. The insertion of Mn^{2+} ions on the Ni^{2+} sites generates competing exchange interactions and local disparate electronic states. The oval symbol denotes the Zhang-Rice triplet. b) Single-crystal X-ray diffraction patterns for $Ni_{1-x}Mn_xPS_3$ showing the (00L) reflections. c) Enlarged view of the (002) Bragg peak as a function of x. d) Evolution of the lattice parameter c with increasing Mn concentration. e) Temperature dependence of the in-plane magnetic susceptibility of $Ni_{1-x}Mn_xPS_3$ (x = 0, 0.05, 0.02, 0.04, 0.06, and 0.08) measured at $\mu_0H = 1$ T. f) Antiferromagnetic ordering temperature T_N and the maximum temperature T_{max} of $\chi(T)$ as a function of x. The dashed gray lines serve as a guide to the eye.

spin-entangled optical excitation called the X-transition, which occurs in the near-infrared spectral range of $E \approx 1.5$ eV below T_N.[6,37–45] The X-transition is characterized by a high degree of linear polarization, with its axis intrinsically tied to the direction of Ni^{2+} spin alignment. Notably, the X-transition signal is strongly suppressed below T_N, alluding to an intrinsic coupling between the electronic states and the underlying magnetic order.

The magneto-exciton coupling is further corroborated by the gradual rotation of the polarization axis under the influence of a magnetic field. Additionally, the field-induced splitting amplitude shows directional dependence relative to the spin orientation.[37,41] This X-transition was initially interpreted as a Zhang-Rice (ZR) singlet exciton.[6,45] Nonetheless, subsequent investigations have proposed alternative scenarios for its origin, including intrinsic band structures with inter-magnetic sublattice excitons and defect-bound excitons.[40–43] Moreover, excitons in NiPS₃ were strongly coupled to phonons, leading to the formation of exciton-phonon bound states and a series of phonon sidebands. A recent study of these spin-entangled excitons in $Ni_{1-x}Cd_xPS_3$ has shown their rapid suppression with only a few percentages of non-magnetic cation substitution, underscoring that the ZR exciton is intriguingly conditioned by the orbital, electronic, and lattice environments of NiS_6 clusters.[44,45] A pressing question that remains unanswered is the extent to which the magneto-exciton retains information about the underlying magnetic structure, especially when the lo-

cal NiS_6 clusters are perturbed through the substitution of metal cations.

MPS_3 compounds are ideally suited for addressing this issue as their magnetism (exchange interactions, easy axis, and magnetic anisotropy) hinges on the species of transition metal M.[16–19] Notably, the end members NiPS₃ and MnPS₃ exhibit contrasting spin models (XXZ-like versus Heisenberg interactions), magnetic structure (zigzag versus Néel type), and magnetic easy axes (a-axis versus c-axis).[28] In this regard, Mn-for-Ni substitution provides an effective means to tune magnetism, thereby presenting a compelling opportunity to scrutinize whether anisotropic excitonic excitations can be used to discern magnetic moment orientations in mixed compounds $Ni_{1-x}Mn_xPS_3$.

In this paper, we combine angle-resolved exciton photoluminescence (PL) with magnetic susceptibility measurements to explore the thermal and substitution behaviors of magneto-excitons in $Ni_{1-x}Mn_xPS_3$ (x = 0–0.1). The rapid damping of magneto-excitons well below T_N and their sensitivity to the introduction of heterogeneous metal ions reveal that the energy and lifetime of these magneto-excitons are dictated by two spin-flip processes and local electronic disparities. Furthermore, we can demonstrate a fundamental correlation between the orientation of PL emission and the underlying magnetic ordering pattern for x = 0–0.06. In particular, the direct optical probing of the magnetic easy axis highlights the potential of $Ni_{1-x}Mn_xPS_3$ in implementing quantum devices based on spin-exciton entangled states.

**ADVANCED
SCIENCE NEWS**

www.advancedsciencenews.com

**ADVANCED
FUNCTIONAL
MATERIALS**

www.afm-journal.de

2. Results

2.1. Structural and Magnetic Properties of $Ni_{1-x}Mn_xPS_3$

We first examine the structure and phase purity of the $Ni_{1-x}Mn_xPS_3$ series using powder X-ray diffraction (XRD). In Figure 1b, the XRD patterns of $Ni_{1-x}Mn_xPS_3$ show sharp (00L) Bragg peaks indexed in the space group of $C2/m$. A closer look at Figure 1c reveals that the (00L) diffraction peaks systematically shift to lower angles with increasing Mn concentration, which is attributed to the larger ionic radius of Mn^{2+} compared to Ni^{2+}. The c-axis lattice parameter was determined by Rietveld refinements of the XRD patterns using FullProf, with the results plotted in Figure 1d. We observe a linear increase of ≈0.3% in the lattice constant c from $x = 0$ to $x = 0.06$, indicating the elongation of the $(Ni,Mn)S_6$ cluster.

Figure 1e presents the temperature-dependent magnetic susceptibility $\chi_{ab}(T)$ of $(Ni_{1-x}Mn_x)PS_3$ measured in an applied magnetic field of $\mu_0 H = 1$ T for $\mu_0 H$ //ab. Since the magnetic easy axis is oriented in the in-plane direction, $\chi_{ab}(T)$ allows us to trace the modifications of magnetic properties of Mn-substituted samples. The Mn-for-Ni substitution results in a systematic increase in $\chi_{ab}(T)$ and a noticeable shift of the broad maximum of $\chi_{ab}(T)$ toward lower temperatures (see the horizontal arrow and the vertical dashed lines). This behavior is, on the one hand, attributed to the significantly larger magnetic moment of Mn^{2+} ions ($S = 5/2; ≈5 \mu_B$) compared to that of Ni^{2+} ions ($S = 1; ≈2 \mu_B$). The enhanced magnetic moment of Mn^{2+} ions not only increases the magnetic susceptibility but also suppresses quantum fluctuations, thereby suppressing short-range magnetic correlations. On the other hand, the exchange interactions between heterogeneous Ni^{2+} and Mn^{2+} ions become more isotropic compared to those in homogenous Ni^{2+} ions and the single-ion anisotropy is reduced for Mn^{2+} ions with a half-filled shell.[46] Overall, these changes in local magnetic interactions promote an increase in the out-of-plane magnetic component, as inferred from the diminished drop of $\chi_{ab}(T)$ below T_N. To quantify this trend, we introduce the decrease in magnetic susceptibility: $\Delta\chi_{ab}(T) = \chi_{ab}(T_N) - \chi_{ab}(T_{min})$, where T_{min} represents the temperature at which $\chi_{ab}(T)$ reaches its minimum. The value of $\Delta\chi_{ab}(T)$ is reduced from 6.66×10^{-4} emu mol^{-1} Oe at $x = 0.00$ to 5.37×10^{-4} emu mol^{-1} Oe at $x = 0.08$. The 19% decrease in $\Delta\chi_{ab}(T)$ highlights the weakening of XY-like magnetic anisotropy. For a precise determination of the underlying spin ordering structure, neutron diffraction measurements are indispensable. Nevertheless, we will demonstrate that, under certain conditions, an optical method can effectively determine the in-plane spin orientations.

We further deduce the antiferromagnetic transition temperature (T_N) from a peak in the temperature derivatives of $\chi_{ab}(T)$ (Figure S1, Supporting Information), and we determine the temperature T_{max}, which corresponds to the maximum of $\chi_{ab}(T)$. As summarized in Figure 1f, both T_N and T_{max} initially undergo a steep, quasi-linear decrease with increasing Mn concentration up to $x = 0.04$, followed by a less steep decrease. Upon substituting 8% Mn for Ni, T_N reduces by 12% and T_{max} by 28%. The close correlation between the two characteristic temperatures in their x dependence can be rationalized by two factors. First, the strength of antiferromagnetic exchange interactions weakens upon the creation of heterogeneous Mn^{2+}- Ni^{2+} superexchange paths. Second, the substitution of Mn for Ni instigates local exchange frustration because Mn^{2+} ions favor antiferromagnetic alignments with three adjacent spins within the ab plane (see the sketch in Figure 1a). In contrast, Ni^{2+} ions prefer to form one antiferromagnetic configuration along the b-axis and two ferromagnetic configurations along the a-axis. This juxtaposition of exchange coupling preferences contributes to the weakening of zigzag magnetic order.

2.2. Photoluminescence of $Ni_{1-x}Mn_xPS_3$

To elucidate the impact of Mn substitution on the behavior of spin-entangled excitons, we conducted PL measurements of $Ni_{1-x}Mn_xPS_3$ under 532 nm continuous-wave laser excitation, as depicted in **Figure 2a**. The PL spectra at $T = 4$ K show an asymmetric sharp profile, characterized by a primary peak (P) along with additional shoulder peaks (S_1 and S_2) on either the lower or higher-energy side in the energy range of 1.474(9)–1.477(7) eV. The observed sharp PL peak of $NiPS_3$ (FWHM≈0.2 meV) is consistent with previously reported data.[6,7,37,38] The weak shoulder peaks are ascribed to the local inhomogeneity of NiS_6 environments as the phonon sidebands appear below the energy of 1.46(2) eV, as exhibited in Figure S2a (Supporting Information). With increasing Mn concentration, the exciton PL profile experiences rapid suppression, broadening, and a blue shift. Furthermore, the well-resolved phonon sidebands observed in the pristine sample merge into broad humps upon Mn-for-Ni substitution (see Figure S2b, Supporting Information). Despite variations in the PL spectral weight, however, no additional peaks were seen, excluding the possibility of phase segregation.

For a quantitative analysis, the PL spectra were fitted with three Lorentzian profiles. The energy and linewidth of the primary peak extracted from these fittings are plotted in Figure 2b,c. A notable increase in peak energy from 1.475 to 1.476 eV is observed at x = 0.01, followed by a nearly linear increase. This is associated with the increase of band gap energy from ≈1.5 eV for $NiPS_3$ to 2.64 eV for $MnPS_3$.[17,47] Concurrently, the PL linewidth undergoes an increase by an order of magnitude from 0.2(1) to 2.5(3) meV as the Mn concentration increases to x = 0.1. A similar inhomogeneous spectral broadening has been reported in $Ni_{1-x}Cd_xPS_3$.[45] Compared to $Ni_{1-x}Mn_xPS_3$, the non-magnetic Cd substitution shows a more pronounced suppression of spin stiffness and T_N. Nonetheless, the degree of the inhomogeneous line broadening up to x = 0.1 remains comparable between $Ni_{1-x}Cd_xPS_3$ and $Ni_{1-x}Mn_xPS_3$ (refer to the comparison in Figure 2b with **Figure 3d** in ref. [45]), indicating that the variation in magnetic order alone is insufficient to account for the rapid destabilization of magneto-excitons. Rather, the alteration in the $(Ni/Mn)S_6$ octahedral environments plays a substantial role in the observed inhomogeneous PL broadening.

Among the purported origins of magneto-excitons in $NiPS_3$, the ZR exciton is highly sensitive to charge redistribution and adjacent spins between Ni d-orbital and S p-orbital electrons. This sensitivity arises because the ZR excitation is formed within a regular arrangement of self-doped $Ni^{2-\delta}S^{2+\delta}_6$ clusters. Thus, the incorporation of distinct MnS_6 octahedra into the uniform lattice of $Ni^{2-\delta}S^{2+\delta}_6$ clusters creates defects and modulates the
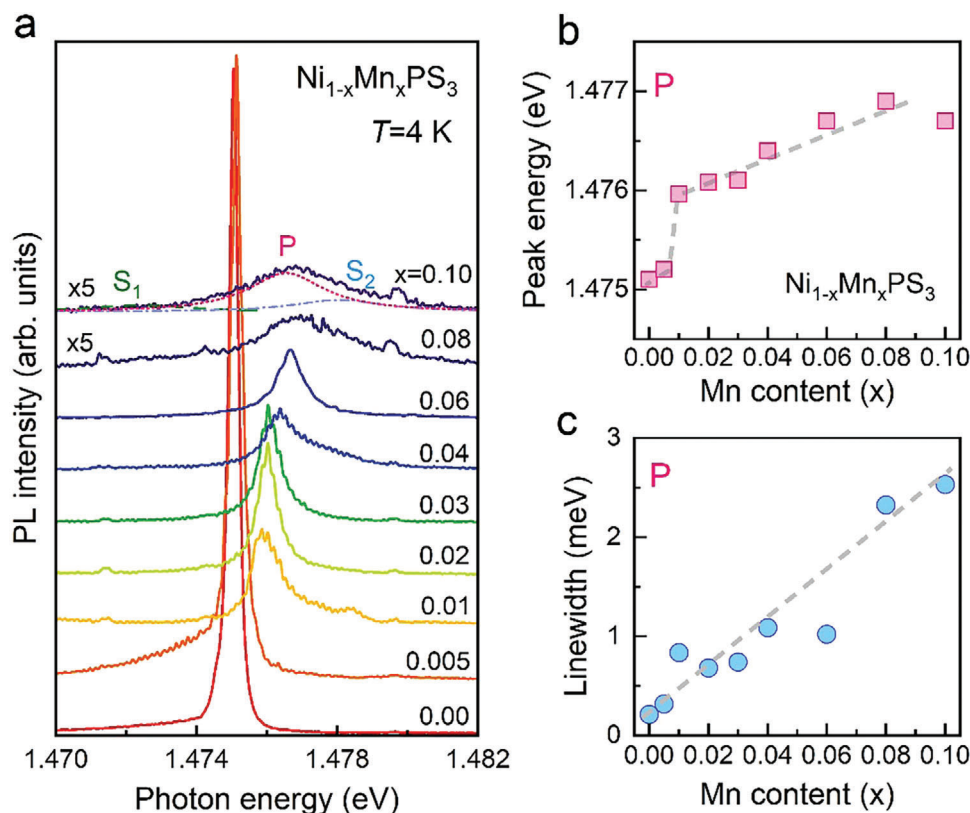
**ADVANCED
SCIENCE NEWS**

www.advancedsciencenews.com

**ADVANCED
FUNCTIONAL
MATERIALS**

www.afm-journal.de

Figure 2. a) PL spectra of $Ni_{1-x}Mn_xPS_3$ at $T = 4$ K as a function of Mn concentration x upon optical excitations at 2.33 eV (532 nm). The spectra are vertically shifted for clarity. The dashed lines denote three Lorentzian profiles: P represents a primary peak and S1 and S2 are secondary peaks. b) Peak energy of the primary peak versus x. c) x dependence of the PL linewidth. The gray dashed lines are a guide to the eye.

charge redistribution between Ni and S orbitals. In view of the ZR exciton scenario, the presence of heterogeneous metallic cations disrupts the entangled electronic and magnetic states within $Ni^{2-\delta}S^{2+\delta}_6$ clusters,[6,45] bringing about the rapid PL broadening.

2.3. Thermal Broadening Processes of PL

We next examine the homogenous broadening of PL as a function of temperature. Figure 3a–c presents the color plots of the PL intensity in the temperature range of $T = 10$–130 K (see Figure S3, Supporting Information for the waterfall plots). As the temperature increases, there is a gradual decrease in the exciton intensity, accompanied by a red shift in its peak energy and a broadening of its linewidth. This trend becomes more pronounced with increasing Mn concentration. The exciton vanishes at a temperature significantly lower than the zigzag ordering temperature, implying that the magneto-exciton is destabilized more quickly than the magnetic order parameter. According to the ZR exciton framework, the optical transitions between ground and excited states involve spin-flip processes.[6] In this scenario, the magneto-exciton is extremely sensitive to thermally populated magnons. In addition to the exciton-magnon interactions, exciton-exciton and exciton-phonon channels also contribute to the homogeneous linewidth.

To elucidate the mechanism underlying homogeneous broadening, we plot the temperature dependence of the peak energy, FWHM, and normalized intensity for samples with x = 0.005, 0.02, and 0.06 in Figure 3d–f. We begin by discussing the exciton-phonon process. At elevated temperatures, the increased phonon population brings about stronger electron−phonon scattering, resulting in the broadening of the PL peak. In this case, the temperature dependence of exciton energies follows the Bose-Einstein occupation factor for phonons[48]

$$E(T) = E(0) - a \left\{ 1 + \frac{2}{\exp(\theta_B/T) - 1} \right\} \tag{1}$$

where $E(0)$ is the exciton energy at $T = 0$ K, a signifies the strength of the exciton-phonon interaction, and θ_B denotes the average phonon temperature. The dashed curves in Figure 3d show the least-square fitting results, with the fitted $E(0)$, a, and θ_B parameters listed in **Table 1**.

Alternatively, we analyze the temperature-dependent linewidth $\Gamma(T)$ using the Bose-Einstein expression

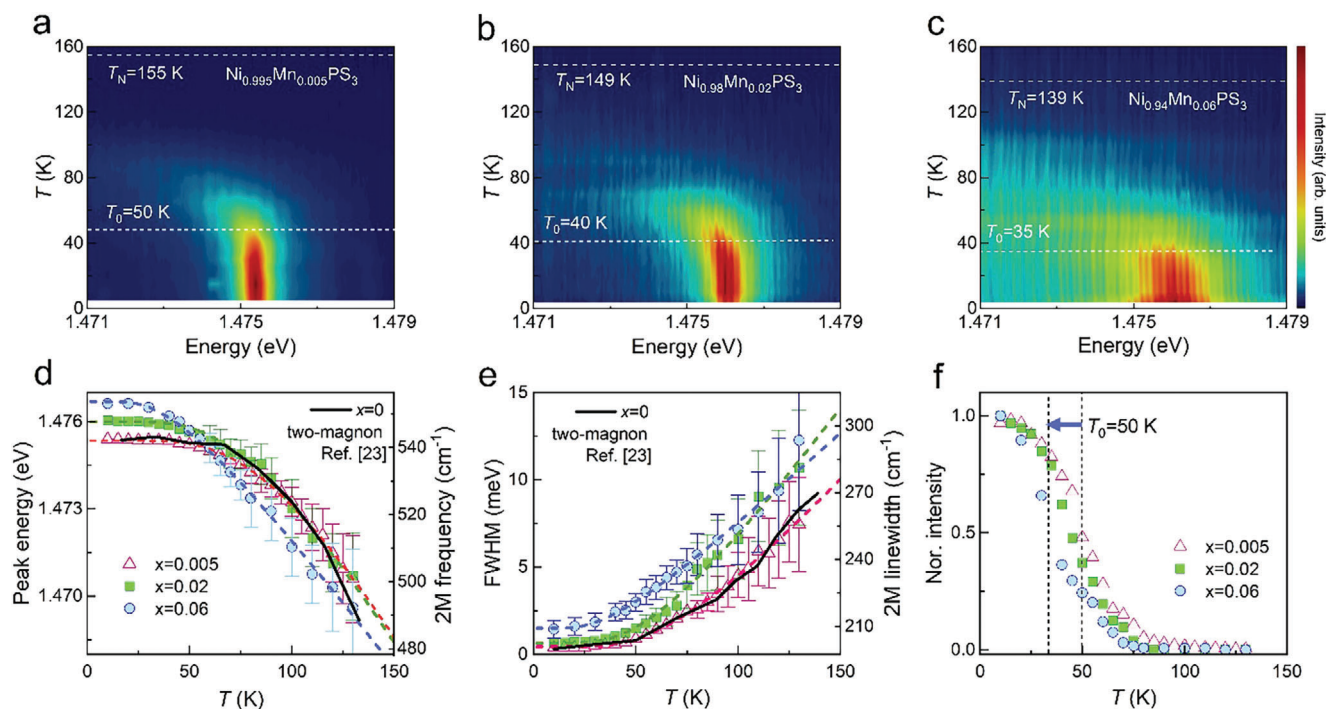$$\Gamma(T) = \Gamma(0) - \frac{\Gamma_{LO}}{[\exp(\theta_{LO}/T) - 1]} \tag{2}$$

**ADVANCED
SCIENCE NEWS**

www.advancedsciencenews.com

**ADVANCED
FUNCTIONAL
MATERIALS**

www.afm-journal.de

Figure 3. a–c) Temperature-dependent PL color map of $Ni_{1-x}Mn_xPS_3$ (x = 0.005, 0.02, and 0.06). The horizontal dashed lines mark the zigzag ordering temperature T_N and the characteristic temperature T_O above which the magneto-excitons undergo a red shift. d) Temperature dependence of the primary (P) peak energy for the x = 0.005, 0.02, and 0.06 samples. e) FWHM as a function of temperature. The solid black line denotes the peak energy and linewidth of the two-magnon scattering reproduced under terms of the CC-BY license.[23] (2019, Springer Nature). The dashed lines are the least-square fits of the data using the Bose-Einstein model as discussed in the text. f) Temperature dependence of the normalized PL intensity.

where the $\Gamma(0)$ term accounts for linewidth broadening due to various factors such as impurities, dislocations, electron interactions, and Auger processes. The term Γ_{LO} is associated with exciton–longitudinal optical (LO) phonon interactions, and θ_{LO} denotes the LO phonon temperature. As illustrated in the dashed lines in Figure 3e, the exciton-phonon mechanism seems to provide a description of the observed linewidth broadening. The deduced broadening parameters are summarized in Table 1. Notwithstanding, the x dependence of the fitting parameters reveals a significant reduction in the strength of the exciton-phonon interactions (a and Γ_{LO}) by approximately three times when the Mn concentration increases from x = 0.005 to 0.06. Concurrently, the average phonon temperature is roughly halved: from $\theta_B = 304 \pm 8$ K ($\theta_{LO} = 211 \pm 10$ K) at x = 0.005 to 123 ± 15 K (107 ± 16 K) at x = 0.06. Given that a small amount of substituted Mn ions barely affects a phonon spectrum (see Figure S4, Supporting Information), these values of θ_B and θ_{LO} appear unrealistic. Additionally, the semiempirical Varshni function is inadequate to explain the temperature dependence of the PL peaks, further invalidating the hypothesis that exciton-phonon interactions are the primary factor (see Figure S5, Supporting Information). In this vein, the strong x dependence of the broadening parameters is likely linked to variations in electronic states, potentially due to a redistribution of electronic density within $Ni^{2-\delta}S^{2+\delta}_6$ clusters.

We further examine the effect of magnon processes on the thermal dynamics of magneto-excitons. Our analysis reveals no significant correlation between the peak energy shift and staggered magnetization (not shown here). However, we observe a notable overlap of the peak energy between excitonic and two-magnon excitations, as highlighted by the solid line in Figure 3d (taken from ref. [23]). This correspondence suggests that the exciton energy is renormalized through two spin-flip processes. Notably, two-magnon Raman processes explain the PL linewidth broadening as well, as depicted in Figure 3e. In consideration of the optical selection rules for ZR excitons, which involve on-site triplet to singlet excitations, spin-conserving two-magnon processes efficiently couple to the magneto-exciton. As shown in

Table 1. Fitting parameters of the Bose–Einstein model that describe the temperature dependences of the exciton energy and linewidth.

Material	$E(0)$ [eV]	a [meV K^{-1}]	θ_B [K]	$\Gamma(0)$ [meV]	Γ_{LO} [meV]	θ_{LO} [K]
x = 0.005	1.497 ± 0.002	22.3 ± 0.4	304 ± 8	0.436 ± 0.064	29.4 ± 3.1	211 ± 10
x = 0.02	1.493 ± 0.003	17.1 ± 0.2	256 ± 12	0.644 ± 0.123	30.1 ± 4.2	173 ± 13
x = 0.06	1.483 ± 0.005	5.8 ± 0.03	123 ± 15	1.499 ± 0.164	11.7 ± 3.6	107 ± 16

**ADVANCED
SCIENCE NEWS**

www.advancedsciencenews.com

**ADVANCED
FUNCTIONAL
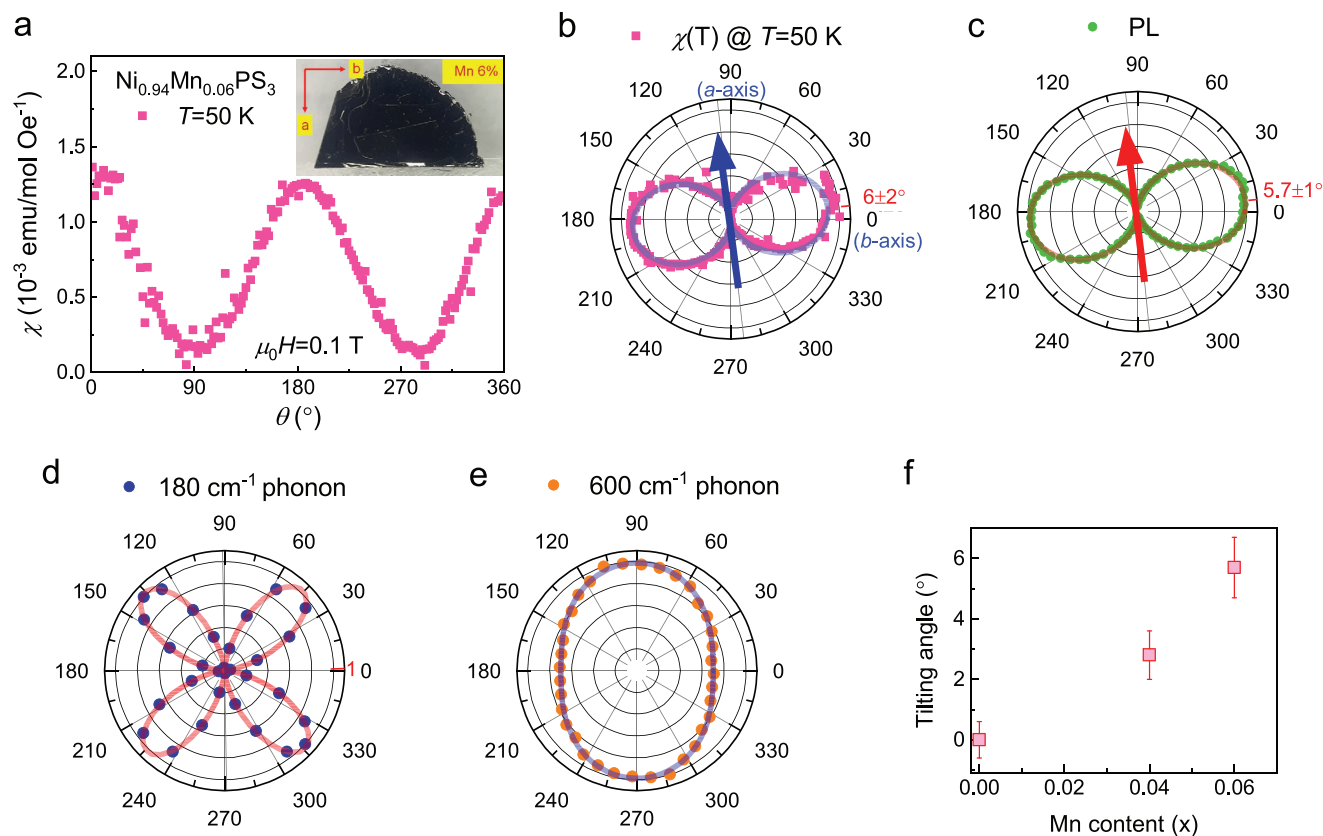MATERIALS**

www.afm-journal.de

Figure 4. a) Angular dependence of the magnetic susceptibility for $x = 0.06$ at $T = 50$ K (pink squares) measured under an in-plane magnetic field of 0.1 T. The inset shows a photo of the sample with labeled crystal axes. b) Polar plots of the magnetic susceptibility at $T = 50$ K c) Polar plot of the integrated PL intensity at $T = 10$ K. The magnetic susceptibility and PL data are overlaid with $\cos^2\theta$ fitting curve (solid line). The arrow indicates the local spin order in the ab plane. d,e) Polar plots of the integrated intensity of 180 and 600 cm^{-1} phonon modes. f) Tilting angle of the local magnetic moments from the a-axis as a function of Mn concentration.

Figure 3f, the PL intensity exhibits a rapid drop to 50% at T_o, coinciding with the onset of the PL energy shift (see the horizontal dashed lines for T_o in Figure 3a–c and the vertical dashed lines in Figure 3f). This correlation indicates a common origin for both the non-radiative recombination process and the PL lifetime. Taken together, the homogenous broadening of PL cannot be adequately captured by the conventional exciton-phonon mechanism. Instead, its rapid dependence on temperature and Mn concentration alludes to the involvement of intriguing spin-flip processes.

2.4. Optical Readout of the Spin Order

Previous studies[6,7] have shown that the ZR exciton is primarily probed through a dipole moment induced by charge redistribution between Ni $3d$ and S $3p$ orbitals. In a pristine sample, both the spin ordering vector and the ferromagnetic spin chain align along the a-axis of the crystal (Figure 1a). Consequently, the emitted PL emits a linearly polarized photon perpendicular to the Néel vector. This anisotropic linear polarization conserves the total spin quantum number along the a-axis, ensuring that any changes in the spin quantum number induced by spin flips are compensated by a magnetic field. It is important to note that

the linear relation between PL polarization and the direction of spin alignment may not be exclusive to the ZR exciton.

To examine the correlation between PL polarization orientation and spin structure in Mn-substituted Ni$_{1-x}$Mn$_x$PS$_3$, we focus on the in-plane magnetic anisotropy of the x = 0.06 sample. The angular dependence of the magnetic susceptibility $\chi(\theta)$ at $T = 50$ K was measured by rotating the sample from the b-axis toward the a-axis, where θ represents the angle between the b-axis and the magnetic field direction. The crystallographic axes were initially determined using Laue X-ray diffraction, and the sample was cut along the b-axis as shown in the inset of Figure 1a. The measured temperature was chosen because the temperature-dependent $\chi(T)$ reaches its minimum at this point (see Figure 1e). As illustrated in **Figure 4**a, $\chi(\theta)$ is maximal near $\theta = 0°$ (b-axis) and reaches its minimum $\theta = 90°$ (a-axis). The polar plot of $\chi(\theta, T = 50$ K) is presented in Figure 4b. The maximal (minimal) $\chi(\theta, T = 50$ K) occurs at an angle offset by 6 ±2° with respect to the b (a) axis, following a $\cos^2\theta$ dependence. Our $\chi(\theta, T = 50$ K) data unveil that the magnetic easy axis is tilted by $\approx 6°$ from the crystalline a-axis. The uncertainty of ±2° mainly arises from backlash in the rotator.

We next turn to angle- and polarization-resolved PL and Raman spectroscopy experiments conducted on the x = 0.06 sample. By performing PL and Raman measurements

**ADVANCED
SCIENCE NEWS**

www.advancedsciencenews.com

**ADVANCED
FUNCTIONAL
MATERIALS**

www.afm-journal.de

simultaneously on the same spot, we can determine the crystal symmetry and the crystallographic axes. The PL polar plot of polarization-resolved PL intensity, shown in Figure 4c, uncovers that the direction of the maximal PL signal occurs at polarization angles rotated by $5.7 \pm 1°$ from the b-axis. To obtain the precise rotation angle, we corrected the initial orientation of the crystal by analyzing two pronounced Raman peaks at 180 and 600 cm^{-1}. Their integrated intensity is plotted as a function of polarization direction, as illustrated in Figure 4d,e, respectively (see Figure S4, Supporting Information for Raman spectra). Analysis of the Raman polar plots reveals a fourfold symmetry for the 180 cm^{-1} mode and a twofold symmetry for the 600 cm^{-1} mode. Through the computation of the Raman matrix element, we are able to ensure that the initial b-axis orientation is within an uncertainty of $\approx 1°$. In this context, the PL data can more accurately identify the orientation of the magnetic easy axis. Within this marginal error, the PL intensity and the $\chi(\theta, T = 50 \text{ K})$ data consistently showcase that the spin ordering vector (red arrow) is rotated by $\approx 5.7 \pm 1°$ from the local spin chain direction for the x = 0.06 sample. For the pristine and x = 0.04 samples, the local spin alignment is rotated by $0 \pm 0.6°$ and $2.8 \pm 0.8°$, respectively (Figure S6, Supporting Information). Figure 4f presents the tilting of the magnetic moment within the basal plane with increasing x, indicating that the spin alignment is modulated in proportion to the degree of competing magnetic anisotropy and interactions, at least in the lightly Mn-substituted $Ni_{1-x}Mn_xPS_3$ compounds.

3. Discussion

Through comprehensive investigations of magneto-excitons in $Ni_{1-x}Mn_xPS_3$, we are able to shed light on their dynamics and characteristics.

Similar to the non-magnetic substituted case of $Ni_{1-x}Cd_xPS_3$,[45] the magneto-exciton undergoes rapid destabilization upon the introduction of a few percentages of magnetic Mn^{2+} cations in $NiPS_3$. Regardless of whether the substitution involves non-magnetic or magnetic elements, even a small amount of heterogeneous metallic cations exerts a drastic impact on the PL intensity and lifetime. A detailed composition and temperature dependence of the PL signal reveals that conventional mechanisms such as exciton-phonon interaction and lattice expansion are insufficient to account for the thermal behaviors of the exciton energy and linewidth. As to magneto-exciton interactions, we observe no relation between the PL energy shift and staggered magnetization (magnetic order parameter). Instead, our PL data show a strong temperature dependence of the PL intensity, peak energy, and linewidth in the magnetically ordered state. Noteworthy is that the characteristic temperature T_o, marking the onset of the PL suppression, corresponds to $\approx 0.3 T_N$. Phenomenologically, we find that the renormalization and damping of two-magnon Raman excitations observed in Raman spectroscopy are correlated with the thermal evolution of the PL energy and linewidth (Figure 3).[23] We recall that the nuclear spin-lattice relaxation rate in the magnetically ordered state is dominated by the two-magnon Raman process.[49] Taken together, the stability of the magneto-exciton is strongly conditioned by spin-conserving two-spin-flip processes and the heterogeneity of local NiS_6 clusters. These characteristics are compatible with the notion of ZR excitons, which are based on

a redistribution of electronic density within $Ni^{2-\delta}S^{2+\delta}{}_6$ clusters and an entangled triplet comprising the $Ni^{2-\delta}$ and $S^{2+\delta}$ spins. In this picture, the entangled spin-excitons become suppressed as soon as the uniformity of $Ni^{2-\delta}S^{2+\delta}{}_6$ cluster lattice is disrupted, and spin order is disturbed by thermally populated magnons. As such, $Ni_{1-x}Mn_xPS_3$ constitutes an exceptional platform for studying the decoherence of quantum entanglement between spin ordering and electronic states using time-resolved spectroscopy.

Taking it one step further, we demonstrate that magneto-excitons can serve as a means for optically reading the magnetic easy axis in lightly Mn-substituted $Ni_{1-x}Mn_xPS_3$, where the magneto-excitations are sufficiently strong to resolve their angular dependence. Introducing Mn^{2+} ions to the Ni^{2+} sites disrupts the ferromagnetic spin alignment pointing to the easy a-axis, as sketched in Figure 1a. This frustration occurs because heterogeneous magnetic cations favor antiferromagnetic exchange interactions. The presence of antiferromagnetic bonds in the ferromagnetic zigzag spin structure causes deviations from the spin orientation along the a-axis, minimizing magnetic energy. As seen from Figure 4f, the gradual rotation of the in-plane magnetic moments is tractable up to x = 0.06. Given that $MnPS_3$ features a Néel-type magnetic structure with the magnetic easy axis directed along the c-axis, the magnetic moments will eventually tilt toward an out-of-plane orientation in heavily Mn-substituted samples.

4. Conclusion

In conclusion, our study provides a comprehensive analysis of the temperature, composition, and angle-resolved exciton photoluminescence in $Ni_{1-x}Mn_xPS_3$ (x = 0–0.1) together with magnetic susceptibility measurements. Notably, the observed spin-entangled excitons in $Ni_{1-x}Mn_xPS_3$ undergo strong renormalization and damping, driven by two primary factors: the two-spin-flip Raman processes and the uniformity of $Ni^{2-\delta}S^{2+\delta}{}_6$ clusters. These findings underscore the critical role of decoherence in both the spin-ordered moments and the local charge redistribution, essential for retaining entangled magneto-excitons. Furthermore, we demonstrate an inherent correlation between the orientation of anisotropic PL emission and the magnetic ordering pattern especially for x = 0.06. Compared to the pristine sample, the magnetic easy axis systematically rotates away from $0 \pm 0.6°$ for x = 0 to $5.7 \pm 1°$ for x = 0.06 with the basal plane. These insights into spin-exciton entangled PL pave the road for further exploration and manipulation of quantum entanglements involving spin and electronic subsystems through light-mediated processes.

5. Experimental Section

Sample Growth and Characterization: High-quality single crystals of $Ni_{1-x}Mn_xPS_3$ (x = 0.005, 0.02, 0.03, 0.04, 0.06,0.08, and 0.1) were successfully grown using chemical vapor transport techniques (CVT), with iodine (I_2) as a transport agent. Initially, polycrystalline powders of $Ni_{1-x}Mn_xPS_3$ were prepared through a solid-state synthesis process. Stoichiometric amounts of high pure Ni (99.99%), Mn (99.99%), phosphorus (99.99%), and sulfur (99.999%) powders were loaded into a silica ampoule within an argon-filled glovebox, then sealed under a high vacuum condition to prevent contamination. The mixed compounds were then heated at 600 °C for 24 h with intermediate grinding performed in the

argon atmosphere to ensure uniformity and phase purity. The synthesized polycrystalline powders were mixed along with 200 mg of iodine (I_2) and sealed by a quartz ampule, 40 cm in length, under a pressure of $\approx 10^{-3}$ Torr. The sealed quartz ampule was kept in a horizontal two-zone furnace. The charge and growth end of the ampule was positioned at the hot and cold zones of the furnace, respectively, at constant temperatures of 700 and 600 °C for 1 week. Upon completion of the growth process, the furnace temperature was cooled down to room temperature at a rate of 2 °C min^{-1}. The high-quality $Ni_{1-x}Mn_xPS_3$ single crystals were harvested from the cold end of the ampule.

For PL and Raman Measurements: Polarization-resolved Raman and PL measurements were carried out to determine the orientations of local crystalline axes and magnetic order. To avoid the uncertainty in sample alignment, the angular dependence of PL and Raman signals were measured simultaneously. A Nd:YAG laser with a wavelength of $\lambda = 532$ nm was used as the excitation source, focused to a spot size of 1 µm^2. The laser power was set to ≈ 500 µW. The samples were mounted inside an optical cryostat to measure the temperature-dependent PL over a temperature range from 4 to 150 K. PL signals were collected in reflection geometry and analyzed using a single grating spectrometer (focal length: 50 cm) equipped with a charge-coupled device (CCD) detector.

Magnetic Susceptibility Measurements: Angular-resolved magnetic susceptibility measurements in the ab plane were performed using Quantum Design MPMS3 SQUID magnetometer (Superconducting Quantum Interference Device). The temperature was fixed at $T = 50$ K and 100 K, and the sample was rotated using the commercial horizontal rotator from Quantum Design. The crystallographic axis was initially determined using Laue X-ray diffraction. The initial orientation was aligned with the crystallographic b-axis at 0° and subsequently rotated in 2° increments. After completing the SQUID measurements, the backlash was found to be 1–2 degrees, indicating an uncertainty of $\approx 2°$ in the reproducibility of the alignment for the magnetic susceptibility measurements.

Supporting Information

Supporting Information is available from the Wiley Online Library or from the author.

Conflict of Interest

The authors declare no conflict of interest.

Data Availability Statement

The data that support the findings of this study are available from the corresponding author upon reasonable request.

[1] K. S. Burch, D. Mandrus, J.-G. Park, *Nature* **2018**, *563*, 47.
[2] M. Gibertini, M. Koperski, A. F. Morpurgo, K. S. Novoselov, *Nat. Nanotechnol.* **2019**, *14*, 408.
[3] S. Yang, T. Zhang, C. Jiang, *Adv. Sci.* **2021**, *8*, 2002488.
[4] X. Jiang, Q. Liu, J. Xing, N. Liu, Y. Guo, Z. Liu, J. Zhao, *Appl. Phys. Rev.* **2021**, *8*, 031305.
[5] S. Y. Kim, T. Y. Kim, L. J. Sandilands, S. Sinn, M.-C. Lee, J. Son, S. Lee, K.-Y. Choi, W. Kim, B.-G. Park, C. Jeon, H.-D. Kim, C.-H. Park, J.-G. Park, S. J. Moon, T. W. Noh, *Phys. Rev. Lett.* **2018**, *120*, 136402.
[6] S. Kang, K. Kim, B. H. Kim, J. Kim, K. I. Sim, J.-U. Lee, S. Lee, K. Park, S. Yun, T. Kim, A. Nag, A. Walters, M. Garcia-Fernandez, J. Li, L. Chapon, K.-J. Zhou, Y.-W. Son, J. H. Kim, H. Cheong, J.-G. Park, *Nature* **2020**, *583*, 785.
[7] D. Afanasiev, J. R. Hortensius, M. Matthiesen, S. MañasValero, M. Šiškins, M. Lee, E. Lesne, H. S. van Der Zant, P. G. Steeneken, B. A. Ivanov, E. Coronado, *Sci. Adv.* **2021**, *7*, eabf3096.
[8] C. A. Belvin, E. Baldini, I. O. Ozel, D. Mao, H. C. Po, C. J. Allington, S. Son, B. H. Kim, J. Kim, I. Hwang, J. H. Kim, J.e-G. Park, T. Senthil, N. Gedik, *Nat. Commun.* **2021**, *12*, 4837.
[9] E. Ergeçen, B. Ilyas, D. Mao, H. C. Po, M. B. Yilmaz, J. Kim, J.-G. Park, T. Senthil, N. Gedik, *Nat. Commun.* **2022**, *13*, 98.
[10] K. Hwangbo, Q.i Zhang, Q. Jiang, Y. Wang, J. Fonseca, C. Wang, G. M. Diederich, D. R. Gamelin, D.i Xiao, J.-H. Chu, W. Yao, X. Xu, *Nat. Nanotechnol.* **2021**, *16*, 655.
[11] X. Wang, J. Cao, H. Li, Z. Lu, A. Cohen, A. Haldar, H. Kitadai, Q. Tan, K. S. Burch, D. Smirnov, W. Xu, S. Sharifzadeh, L. Liang, X. Ling, *Sci. Adv.* **2022**, *8*, eabl7707.
[12] J. Liu, Y. Wang, Y. Fang, Y. Ge, X. Li, D. Fan, H. A. Zhang, *Adv. Electron. Mater.* **2019**, *5*, 1900726.
[13] J. Chu, F. Wang, L. Yin, L. Lei, C. Yan, F. Wang, Y. Wen, Z. Wang, C. Jiang, L. Feng, J. Xiong, Y. Li, J. He, *Adv. Funct. Mater.* **2017**, *27*, 1.
[14] R. N. Jenjeti, R. Kumar, M. P. Austeria, S. Sampath, *Sci. Rep.* **2018**, *8*, 1.
[15] R. N. Jenjeti, R. Kumar, S. Sampath, *J. Mater. Chem. A* **2019**, *7*, 14545.
[16] G. Leflem, R. Brec, G. Ouvard, A. Louisy, P. Segransan, *J. Phys. Chem. Solids* **1982**, *43*, 455.
[17] R. Brec, *Solid State Ion.* **1986**, *22*, 3.
[18] N. Kurita, K. Nakao, *J. Phys. Soc. Jpn.* **1989**, *58*, 610.
[19] P. A. Joy, S. Vasudevan, *Phys. Rev. B* **1992**, *46*, 5425.
[20] N. Chandrasekharan, S. Vasudevan, *J. Phys.: Condens. Matter* **1994**, *6*, 4569.
[21] A. R. Wildes, V. Simonet, E. Ressouche, G. J. Mcintyre, M. Avdeev, E. Suard, S. A. J. Kimber, D. Lançon, G. Pepe, B. Moubaraki, T. J. Hicks, *Phys. Rev. B.* **2015**, *92*, 224408.
[22] D. Lançon, R. A. Ewings, T. Guidi, F. Formisano, A. R. Wildes, *Phys. Rev. B.* **2018**, *98*, 134414.
[23] K. Kim, S. Y. Lim, J.-U. Lee, S. Lee, T. Y. Kim, K. Park, G. S. Jeon, C.-H. Park, J.-G. Park, H. Cheong, *Nat. Commun.* **2019**, *10*, 345.
[24] H.-S. Kim, K. Haule, D. Vanderbilt, *Phys. Rev. Lett.* **2019**, *123*, 236401.
[25] C. Lane, J.-X. Zhu, *Phys. Rev. B.* **2020**, *102*, 075124.
[26] T. Olsen, *J. Phys. D: App. Phys.* **2021**, *54*, 314001.
[27] T. Y. Kim, C.-H. Park, *Nano Lett.* **2021**, *21*, 10114.
[28] R. Basnet, A. Wegner, K. Pandey, S. Storment, J. Hu, *Phys. Rev. Mater.* **2021**, *5*, 064413.
[29] H. Cui, S. Yun, K. J. Lee, C. Lee, S. H. Chang, Y. Lee, H. H. Lee, K. Raju, K. Moovendaran, R. Sankar, K.-Y. Choi, *Phys. Rev. Mater.* **2021**, *5*, 124008.

[30] M. Yan, Y. Jin, Z. Wu, A. Tsaturyan, A. Makarova, D. Smirnov, E. Voloshina, Y. Dedkov, *J. Phys. Chem. Lett.* **2021**, *12*, 2400.

[31] A. R. Wildes, J. R. Stewart, M. D. Le, R. A. Ewings, K. C. Rule, G. Deng, K. Anand, *Phys. Rev. B.* **2022**, *106*, 174422.

[32] R. Basnet, K. M. Kotur, M. Rybak, C. Stephenson, S. Bishop, C. Autieri, M. Birowska, J. Hu, *Phys. Rev. Res.* **2022**, *4*, 023256.

[33] F. Bougamha, S. Selter, Y. Shemerliuk, S. Aswartham, A. Benali, B. Büchner, H.-J. Grafe, A. P. Dioguardi, *Phys. Rev. B.* **2022**, *105*, 024410.

[34] K. Mehlawat, A. Alfonsov, S. Selter, Y. Shemerliuk, S. Aswartham, B. Büchner, V. Kataev, *Phys. Rev. B.* **2022**, *105*, 214427.

[35] K. Synnatschke, J. Dinter, A. Müller, D. Tiede, L. Spillecke, S. Shao, D. Kelly, J. Konecny, B. Konkena, M. McCrystall, N. Saigal, U. Wurstbauer, W. Bensch, Z. Sofer, J. N. Coleman, R. Klingeler, S. Haigh, *2D Mater.* **2023**, *10*, 024003.

[36] S. Lee, J. Park, Y. Choi, K. Raju, W.-T. Chen, R. Sankar, K.-Y. Choi, *Phys. Rev. B.* **2021**, *104*, 174412.

[37] X. Wang, J. Cao, Z. Lu, A. Cohen, H. Kitadai, T. Li, Q. Tan, M. Wilson, C. H. Lui, D. Smirnov, S. Sharifzadeh, X.i Ling, *Nat. Mater.* **2021**, *20*, 964.

[38] C. H. Ho, T. Y. Hsu, L. C. Muhimmah, *npj 2D Mater. Appl.* **2021**, *5*, 8.

[39] F. Dirnberger, R. Bushati, B. Datta, A. Kumar, A. H. MacDonald, E. Baldini, V. M. Menon, *Nat. Nanotechnol.* **2022**, *17*, 1060.

[40] D. S. Kim, D. Huang, C. Guo, K. Li, D. Rocca, F. Y. Gao, J. Choe, D. Lujan, T.-H. Wu, K.-H. Lin, E. Baldini, L. Yang, S. Sharma, R. Kalaivanan, R. Sankar, S.-F. Lee, Y. Ping, X. Li, *Adv. Mater.* **2023**, *1735*, 2206585.

[41] D. Jana, P. Kapuscinski, I. Mohelsky, D. Vaclavkova, I. Breslavetz, M. Orlita, C. Faugeras, M. Potemski, *Phys. Rev. B.* **2023**, *108*, 115149.

[42] A. Shcherbakov, K. Synnatschke, S. Bodnar, J. Zerhoch, L. Eyre, F. Rauh, M.s W. Heindl, S. Liu, J. Konecny, I. D. Sharp, Z. Sofer, C. Backes, F. Deschler, *ACS Nano* **2023**, *17*, 10423.

[43] H. J. Kim, K.-S. Kim, *New J. Phys.* **2023**, *25*, 083029.

[44] T. Klaproth, S. Aswartham, Y. Shemerliuk, S. Selter, O. Janson, J. van den Brink, B. Büchner, M. Knupfer, S. Pazek, D. Mikhailova, A. Efimenko, R. Hayn, A. Savoyant, V. Gubanov, A. Koitzsch, *Phys. Rev. Lett.* **2023**, *131*, 256504.

[45] J. H. Kim, W. K. Na, J. H. Kim, P. J. Park, K. Zhang, I. Hwang, Y.-W. Son, J. H. Kim, H. Cheong, J.-G. Park, *Nano Lett.* **2023**, *23*, 10189.

[46] A. Elghandour, L. Gries, L. Singer, M. Hoffmann, S. Spachmann, M. Uhlarz, K. Dey, R. Klingeler, *Phys. Rev. B.* **2023**, *17108*, 014406.

[47] S. Gnatchenko, I. Kachur, V. Piryatinskaya, Y. M. Vysochanskii, M. Gurzan, *Low Temp. Phys.* **2011**, *37*, 144.

[48] P. Lantenschlager, M. Garriga, S. Logothetidis, M. Cardona, *Phys. Rev. B* **1987**, *35*, 9174.

[49] B. Beeman, P. Pincus, *Phys. Rev.* **1968**, *166*, 359.